Eksploatacja i Niezawodnosc – Maintenance and Reliability
Volume 28 (2026), Issue 4
journal homepage: http://www.ein.org.pl

Article citation info:
Li X, He G, Wang K, Fu Y, Resonance-induced ballistic premature detonation in fuzes: mul-ti-evidence diagnosis and assembly-based vibration suppression, Eksploatacja i Niezawodnosc – Maintenance and Reliability 2026: 28(4) http://doi.org/10.17531/ein/218283

Resonance-induced ballistic premature detonation in fuzes: mul-ti-evidence diagnosis and assembly-based vibration suppression

Indexed by:
Web of Science Group

Xinmin Li[a], Guanglin He[a,*], Kaipeng Wang[a], Yuzhe Fu[a]

[a] National Key Laboratory of Proximity Detection and Control, Beijing Institute of Technology, China

Highlights

- A four-level evidence chain method for fuze fault diagnosis is proposed.
- Revealed the resonance failure mechanism of the 82 mm mortar fuze.
- Multi-source data fusion improves diagnostic reliability under field conditions.
- The suppression scheme has the characteristics of low cost and simple implementation.

Abstract

This study investigates premature detonation failures in an 82 mm mortar projectile fuze using a multiscale framework combining fault tracing, time-frequency analysis, finite element simulation, and modal testing. After eliminating software, hardware, and environmental pathways through fault tree analysis, structural dynamic anomalies were identified as the primary failure mechanism. Time-frequency analysis revealed failures occurring between 34.59 and 35.17 seconds, coinciding with the turbine generator's excitation band of 1160–1240 Hz. Simulations predicted a local bending modal frequency of 1216 Hz, validated experimentally at 1204.10 Hz (0.98% deviation). The third-order mode showed high sensitivity to assembly parameters, with frequency variations reaching 271.5 Hz. A dual-side washer configuration shifted the modal frequency to 985.9 Hz and reduced response amplitudes by 56.44%. Optimized wave springs stabilized frequencies between 987.2 and 1064.6 Hz with 39.39% additional amplitude reduction. Field testing of 40 units validated the "stiffness regulation–interface dissipation" strategy.

Keywords

fuze premature burst, structural resonance, multiscale analysis, modal sensitivity, interface dissipation

1. Introduction

Premature in-flight detonation of artillery fuzes represents one of the most critical failure modes in munitions systems, directly compromising weapon platform reliability and operator safety. Structural resonance problems are prevalent in various mechanical systems, and studies have demonstrated that modal parameters significantly affect system performance and operational safety [1,2]. During testing of a certain 82 mm mortar projectile model equipped with an electronic proximity fuze featuring turbine generator power supply, five incidents of premature detonation occurred—far exceeding military acceptance requirements—making it imperative to elucidate the underlying mechanisms and develop feasible engineering countermeasures [3].

Existing research has achieved progress in electronic interference mitigation [4], structural reinforcement [5], and vibration control of munitions systems [6]. The theoretical basis for resonance-induced fuze failures can be traced to classical mechanical vibration theory: Den Hartog [7] established that coincidence between excitation frequencies and structural natural frequencies leads to amplified dynamic response, a principle that Harris [8] subsequently documented across

---

(*) Corresponding author.
E-mail addresses: XM. Li (ORCID: 0009-0001-5972-8827) li_xinmin18@163.com, G. He, heguanglin@bit.edu.cn, K. Wang, 3120215105@bit.edu.cn, Y. Fu, 3120230161@bit.edu.cn

diverse military vibration environments. Ewins [9] developed systematic experimental modal analysis methodologies that remain foundational for resonance identification in complex structures. Zhang et al. [10] applied these principles to fuze systems, suggesting that resonance or multimodal coupling may induce premature detonations, though their analysis remained qualitative. Recent work on turbofan blade fatigue has demonstrated successful integration of resonance mode analysis with dangerous resonance point identification [2], while finite element analysis combined with experimental validation has proven effective for structural failure prevention [11].

The role of assembly parameters in structural dynamics has attracted considerable attention. Chen et al. [12] developed optimization methods for bolted joint stiffness considering preload effects, while subsequent studies [13,14,15] revealed that interface stiffness variations can induce significant modal frequency shifts. Interface dissipation strategies, proven effective in rotating machinery applications [1,16], offer potential pathways for vibration suppression. Active control methods employing feedback controllers represent current research frontiers [1], alongside reliability estimation under small-sample conditions [17] and Bayesian network approaches for fault tree analysis [18]. International developments in structural health monitoring [19–21] and multi-scale fault diagnosis [22] have advanced feature extraction methodologies, with frequency-domain methods such as PolyMAX [9,23] now widely adopted for modal parameter identification.

Nevertheless, conventional fuze malfunction diagnosis presents inherent methodological limitations. Post-mortem fragment analysis, while widely employed in failure investigation, provides evidence only after destructive events and precludes controlled verification on failed specimens [24]. Environmental qualification testing per GJB 573B-2020 evaluates fuze response to standardized excitation profiles, yet these profiles may not replicate the specific flight conditions—such as turbine generator excitation bands—that trigger field failures [25]. Statistical reliability assessment based on accumulated failure data can quantify failure probabilities but requires extensive sample sizes often unavailable for low-frequency catastrophic events, and fundamentally cannot establish causal mechanisms linking design parameters to observed failures [26].

These single-source approaches share a common limitation: when the underlying failure mechanism involves complex interactions among structural dynamics, assembly conditions, and operational excitation, multiple potential causes may produce indistinguishable signatures, and sequential hypothesis elimination becomes inefficient. Existing literature rarely establishes rigorous closed-loop connections between complete ballistic time-frequency observations and modal identification, lacking a quantitative analytical framework for the causal chain: assembly parameter variation → modal frequency shift → excitation coupling → response amplification. Unlike single-method approaches that rely solely on data-driven techniques [22] or isolated experimental validation [1], a comprehensive framework integrating fault tree analysis for systematic failure decomposition, time-frequency analysis for transient signal characterization, finite element simulation for mechanism prediction, and experimental modal analysis for physical validation remains absent in the literature, particularly for ordnance systems where resonance-induced failures pose severe safety risks.

To address this research gap, the present study establishes a multi-scale analytical framework—fault tracing → time-frequency mining → numerical simulation → experimental modal validation—using an 82 mm artillery fuze as the case study. Through integration of multi-source evidence, this research quantifies the influence of assembly parameters on modal characteristics and proposes a validated engineering vibration suppression solution.

Compared to existing studies, the novelty and contributions of this work include:

(1) Establishment of a four-tier evidence chain (FTA – time-frequency analysis – FEA – modal testing) to achieve high-confidence fault source identification. Unlike single-method fault diagnosis approaches that focus on either uncertainty quantification in fault trees [18] or data-driven pattern recognition [22], this framework provides closed-loop verification from phenomenon to mechanism through multi-source evidence cross-validation.

(2) Quantification of the mechanisms by which assembly conditions influence fuze modal frequencies. While Chen et al. [12] demonstrated through modal simulations

that preload variations affect the dynamic characteristics of bolted connections, this work extends assembly parameter analysis to threaded fuze-projectile interfaces under ballistic loading conditions, revealing the sensitivity of high-frequency local bending modes to interface stiffness variations with frequency shifts reaching 271.5 Hz.

(3) Proposed a synergistic "stiffness regulation-interface dissipation" vibration suppression strategy achieving 56.44% response amplitude reduction. Unlike active control methods employing piezoelectric actuators and feedback controllers [1], this passive approach combines frequency-shifting through elastic washers with interface friction dissipation, providing a low-cost, maintenance-free engineering solution suitable for expendable ordnance applications.

(4) Provision of a reproducible methodological framework for equipment fault diagnosis under small-sample conditions. By integrating multi-source physical evidence rather than relying solely on statistical inference from limited failure data, this framework achieves high-confidence fault identification with only five failure samples, offering a systematic approach applicable to similar resonance-induced failure diagnosis in safety-critical mechanical systems.

2. Methodology

2.1. Multi-scale validation framework

To elucidate the mechanisms underlying resonance-induced ballistic detonation in artillery fuzes and achieve closed-loop verification from fault tracing through vibration suppression design, this study establishes a multi-scale integrated validation framework (Figure 1). Following the analytical progression from phenomenon to mechanism and from analysis to verification, this framework integrates Fault Tree Analysis (FTA), complete ballistic trajectory data mining, Finite Element Analysis (FEA), and experimental modal analysis to construct a comprehensive evidence chain [27,28].

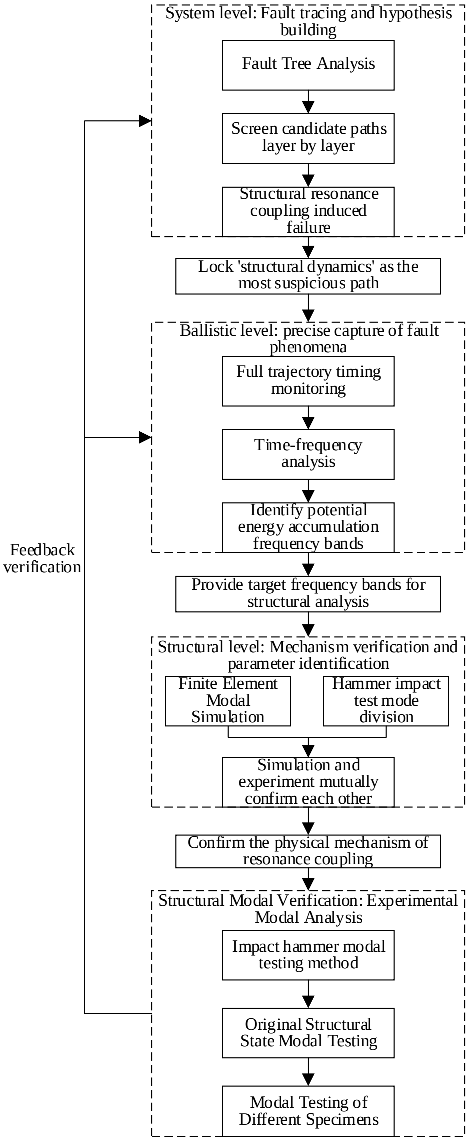

Figure 1. Multi scale research framework diagram of fuze resonance mechanism.

2.2. System-level fault root cause analysis: fault tree analysis

FTA serves as a top-down deductive rea-soning methodology that systematically de-composes system-level failure events into fundamental causal events through logical gate structures [29–31]. This study employs FTA as a qualitative root cause analysis tool to com-prehensively map potential causal pathways for premature fuze detonation and evaluate inves-tigation priorities [32,33]. Based on the fuze system's operational principles, structural composition, and ballistic environment char-acteristics, a comprehensive fault tree model was constructed (Figure 2)，the corresponding fault tree events for fuze ballistic detonation are listed in Table 1.

Based on FTA analysis, potential causes of premature ballistic detonation were categorized into four types: (1) software malfunctions including detonation logic errors and program anomalies; (2) hardware defects such as inertial switch misfiring; (3) environmental interfer-ence effects including electromagnetic com-patibility issues; and (4) Structural dynamics anomalies (resonance-induced). Corresponding troubleshooting tests were designed for each pathway, including: - 91-round multi-munition verification tests - 7-round environmental qualification tests - Batch inspection of inertial switches - Multi-munition comparative tests in the same field Detailed troubleshooting results are presented in Section3.1.

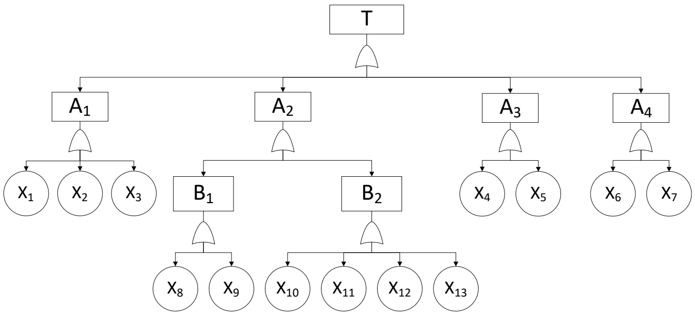

Figure 2. Ballistic explosion fault tree.

Table 1. Fault tree events of ballistic burst of 82 mm mortar projectile fuze.

Event ID	Superior events	Event Name
T	--	Fuze Ballistic Detonation
A1	T	Software Failure
A2	T	Hardware Failure
A3	T	Environmental Interference
A4	T	Structural Dynamics Anomaly
B1	A2	Inertial Switch Failure
B2	A2	Structural Component/Connection Failure
X1	A1	Program Runaway
X2	A1	Program Anomaly
X3	A1	Software Version Error
X4	A3	Abnormal Noise Surge
X5	A3	Interference Signal Coupling
X6	A4	Structural Resonance
X7	A4	Incompletely Torqued Fuze
X8	B1	Inertial Switch Not Qualified
X9	B1	Inertial Switch Mechanical Fatigue
X10	B1	Turbo-generator Damage
X11	B2	Conductor Fatigue Fracture
X12	B2	Solder Joint Fatigue Failure
X13	B2	Electronic Component Failure

Based on FTA-identified structural dynamic anomaly paths, this paper proposes a three-tier progressive validation strategy:

(1) Time-frequency domain evidence layer: Extract time-frequency characteristics from vibration signals in actual ballistic data to identify narrowband energy concentration phenomena and determine the presence of resonant frequency bands.

(2) Simulation Prediction Layer: Numerical simulations predict the natural frequencies and mode shapes of the fuze-projectile structure to assess coupling risks with ballistic excitation bands.

(3) Experimental Verification Layer: Experimental measurements of actual modal parameters cross-validate simulation predictions and assess the impact of assembly conditions on modal characteristics.

These three verification layers mutually corroborate each other, collectively forming a complete argumentation chain from "failure phenomena → virtual simulation → physical mechanisms."

2.2.1. Full ballistic time-frequency analysis

To investigate structural dynamic anomalies, this study conducted full trajectory timing monitoring of a certain type of 82mm mortar projectile at the shooting range. The environmental conditions on the day of testing were as follows: ambient temperature of 18.3°C, atmospheric pressure of 101.325 kPa, and relative humidity of approximately 45%.Preprocess and perform time-frequency analysis on the internal voltage acceleration information and turbine excitation frequency band of the recovered fuze. To precisely quantify failure characteristics, an acoustic delay correction model was employed to reproduce failures. The timing at observation points T can be derived from (Figure 3):

$$T = t + \frac{\sqrt{H^2+[M^2+(S-S_t)^2]}}{v_{sound}} \tag{1}$$

where H represents the detonation point altitude, S_t denotes the horizontal distance to detonation , S is the total range, M is the perpendicular distance from the observation point to the ballistic trajectory, and v_{sound} is the speed of sound taken as 342 m/s. The parameters S, S_t and H were obtained using ballistic calculation software, while M was determined by measuring the delay between explosion flash and acoustic signature.

To verify whether fuze-projectile inter-face assembly conditions could induce prem-ature detonation, comparative assembly state tests were conducted based on the failure reproduction methodology. Table 2 summarizes the test matrix examining natural installation versus wrench-tightened configurations.

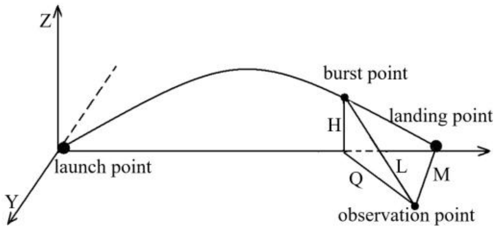

Figure 3. Schematic diagram of time calculation for observation points.

Table 2. Comparison and verification test table for assembly status.

Test No.	Assembly Configuration	Test No.	Assembly Configuration
1	Natural Installation	6	Natural Installation
2	Natural Installation	7	Wrench-Tightened
3	Natural Installation	8	Wrench-Tightened
4	Natural Installation	9	Wrench-Tightened
5	Natural Installation	10	Wrench-Tightened

Time-frequency analysis of complete ballistic accelerometer data aimed to extract fault-associated frequency bands from measured signals, providing data-level evidence for fault source identification. A triaxial accelerometer was mounted on the fuze body without altering the system center of gravity, featuring a measurement range of ±500g, sensitivity of 50 mV/g, and sampling frequency of 10 kHz.

2.2.2. Structural modal analysis: finite element and modal simulation

A finite element dynamic model was developed based on the geometric configuration and material properties of the fuze-projectile assembly to predict inherent modal characteristics (Figure 4). Three-dimensional modeling was performed according to actual component dimensions, with local mesh refinement applied to critical bending sections of the fuze to ensure computational convergence and accuracy. Material properties for all components were set according to specifications, as shown in Table 3. To maintain consistency with the test state, boundary conditions were set as free-state in the simulation.

Modal analysis focuses on two types of objectives: the first-order bending mode of the complete projectile body, extracted through eigenvalue analysis to characterize low-frequency global dynamic characteristics of the structure; and identification of high-frequency local bending modes primarily associated with the fuze, evaluating their resonance risk with the turbine excitation frequency band.

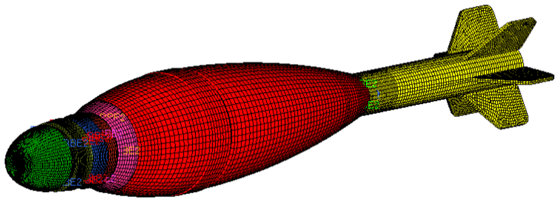

Figure 4. Structural Finite Element Network.

Table 3. Structural material properties.

Component	Material	Young's Modulus E	Poisson's ratio
Fuze-body	Hard-aluminum alloy	70GPa	0.3
Projectile body	Rare earth spheroidal graphite cast iron	150GPa	0.3

2.2.3. Structural modal verification: experimental modal analysis

2.2.3.1. Test principle

Modal testing is conducted on specimens using the hammer impact method. Tests are performed under free-hanging conditions to simulate the boundary conditions in the simulation, as shown in Figure 5.

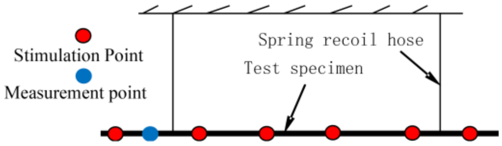

Figure 5. Schematic diagram of hammer impact test.

ICP three-axis accelerometers are positioned at the fuze test points, and a PCB Piezotronics Model 086C02 modally tuned impulse hammer was used for excitation (measurement range: ±444 N pk, sensitivity: 11.2 mV/N, resonant frequency: ⩾22 kHz). Impact forces of approximately 300 N were applied at seven excitation points. Modal parameters were extracted from each measurement set using the PolyMAX algorithm. Mode identification was performed using Modal Assurance Criterion (MAC > 0.9 indicating high consistency) and Modal Overcomplexity (MOV > 0.95 indicating physical modes) as quality indicators. The identified target local modes exhibited high MAC values (>0.95), with MOV values consistent with physical modes, confirming measurement reliability. The LMS Test.Lab modal analysis software from LMS of Belgium is used for data acquisition, with a sampling rate set to 10 kHz. Each measurement point is tested five times to ensure data reliability. The specimen and instrumentation layout is shown in Figure 6.

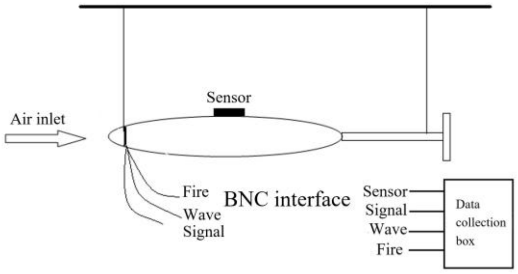

Figure 6. Layout diagram of test specimen components.

2.2.3.2. Modal parameter identification: frequency-domain system identification methods

Modal parameters are extracted from mutual power spectrum Syy using standard PolyMAX procedures [34,35].

Determining Modal Shapes Using the LSFD Method [36]:

$$\widehat{\boldsymbol{H}}(\omega) = \sum_{r=1}^{N_m} \frac{\boldsymbol{v}_r \boldsymbol{l}_r^T}{j\omega-\lambda_r} + \frac{\boldsymbol{v}_r^* \boldsymbol{l}_r^H}{j\omega-\lambda_r^*} + \frac{\boldsymbol{LR}}{(j\omega)^2} + \boldsymbol{UR} \tag{2}$$

λ_r represents the pole of the kth order for the system, where * denotes the complex conjugate; $\boldsymbol{v}_r$ is the modal matrix, $\boldsymbol{l}_r^T$ is the modal participation factor. Considering the modal influence above and below the frequency band range, $\boldsymbol{LR}$ and $\boldsymbol{UR}$ are the upper residual matrix and lower residual matrix, respectively.

Mutual power spectrum $\boldsymbol{S}_{yy}$ form:

$$\boldsymbol{S}_{yy}(j\omega) = \sum_{r=1}^{N} \left(\frac{\boldsymbol{v}_r \boldsymbol{g}_r}{j\omega - \lambda_r} + \frac{\boldsymbol{v}_r^* \boldsymbol{g}_r^*}{j\omega - \lambda_r^*} + \frac{\boldsymbol{g}_r \boldsymbol{v}_r}{-j\omega - \lambda_r} \right.$$
$$\left. + \frac{\boldsymbol{g}_r^* \boldsymbol{v}_r^*}{-j\omega-\lambda_r^*} \right) + \frac{\boldsymbol{LR}}{j\omega} + j\omega \boldsymbol{UR} \tag{3}$$

where $\boldsymbol{g}_r$ is the working participation factor of mode r.

The order of the power spectrum model is twice that of the frequency response function model. The objective of working mode analysis is to identify the right-hand side of equation (3).

Three types of indicators are used to cross-validate modal identification quality: 1) frequency response function reconstruction to verify goodness of fit; 2) Modal Assurance Criterion (MAC) to assess modal vector consistency (MAC > 0.9 indicates high consistency); 3) Modal Complexity (MOV) to distinguish physical modes from noise (MOV > 0.95 indicates physical mode).

$$[H(\omega)] = \sum_{r=1}^{N} \left(\frac{[A]_r}{j\omega-P_r} + \frac{[A^*]_r}{j\omega-P_r^*} \right) \tag{4}$$

MAC [37]:

$$MAC = \frac{\left|\{\Phi^*\}_r^T \{\Phi\}_s\right|^2}{\left(\{\Phi^*\}_r^T \{\Phi\}_r\right)\left(\{\Phi^*\}_s^T \{\Phi\}_s\right)} \tag{5}$$

MOV:

$$\mathrm{MOV}_r = \frac{\sum_{i=1}^{N_0} w_i a_{ir}}{\sum_{i=1}^{N_0} w_i} \times 100\% \tag{6}$$

2.2.3.3. Modal testing of different specimens

To validate the accuracy and reliability of finite element modal simulation results, physical measurements are necessary to confirm the predicted natural frequencies. Considering factors such as manufacturing tolerances and assembly variations that can lead to differences between individual specimens, impact hammer modal testing is conducted according to its fundamental principles. Five fuze specimens (S1, S2, S3, S4, S5), identical in structural state to the original ammunition, are selected for this purpose. To ensure consistency between the experimental and simulation boundary conditions—specifically, the free-free condition used in the finite element analysis—the specimens are suspended in a free-free manner. This suspension method minimizes frequency shift errors caused by external constraints. The suspension points and method are kept consistent across all five specimens.

The testing aims to acquire the frequency of the target local mode, FRFs along with their coherence functions, the first three natural frequencies, and Modal Assurance Criterion (MAC) diagrams. A statistical analysis of the modal frequency shifts and amplitude variations between the different specimens is then performed. This analysis provides a reliable experimental basis for subsequent vibration suppression decisions.

Five specimens (S1-S5) from the same manufacturing batch, all passing quality inspections without prior testing or damage, were selected.

3. Fault source identification and resonance mechanism

3.1. Fault pathway investigation results

Based on Section 2.2 FTA, this paper uses file reports and test evidence to qualitatively investigate candidate branches item by item, with the following results:

1. Environmental interference: Ruled out. Two other projectile types tested simultaneously at the same site showed no detonation, excluding site-specific environmental factors.
2. Software malfunction: Ruled out. Software version verified correct; only 5 of 91 qualification launches exhibited detonation, inconsistent with software-induced

patterns.

(3) Hardware failure: Ruled out. All inertial switches passed factory inspections; flight data showed no overloads exceeding 150g; Circuit tests confirmed normal functionality in all units after transportation vibra-tion tests, 1.5m drop tests, and 15-tooth hammer impact tests with the head oriented upward [25].

(4) Structural dynamics anomalies: Identified as primary suspect. Acoustic delay analysis (Table 2) revealed loosened fuzes detonated at 33.30 s versus 37.31 s for wrench-tightened units, indicating assembly tightness affects detonation timing. Thread preload loss reduces connection stiffness, shifting modal frequencies downward [13,14]. If this shift coincides with the turbine generator excitation band, resonance may occur.

3.2. Ballistic time-frequency characteristic analysis

Full-trajectory data mining reveals the time-frequency domain co-occurrence between ballistic premature detonation events and turbine excitation. After sound wave delay correction, the detonation times of two fault samples both fall within the narrow window of 34.59-35.17 s, corresponding to the turbine generator working frequency band of 1160-1240 Hz, constituting key evidence of "excitation-response synchronization," as shown in Figures 7 and 8. Unlike traditional fuze fault analysis that only focuses on instantaneous overload, through joint time-frequency domain analysis, dynamic correlation positioning between excitation source and structural response is achieved, providing precise frequency and time benchmarks for subsequent modal testing.

According to acoustic theory [38], The influence of atmospheric parameter fluctuations on time calibration accuracy was evaluated as follows: The temperature coefficient of sound velocity is 0.6 m/s/°C. For the observed temperature variations at the test range (within ±5°C of the nominal 18°C), the corresponding sound velocity uncertainty is ±3 m/s, representing a relative uncertainty of ±0.88%. For acoustic propagation over observation distances of approximately 1473 m (Perform 5 ground sound delay statistics based on Figure 1, and take the average of the distance M), this velocity uncertainty translates to time calibration errors of approximately ±0.04 seconds. This uncertainty is negligible compared to the 0.58-second time window (34.59–35.17 s) within which premature detonation failures were observed, and does not affect the validity of the time-frequency correlation.

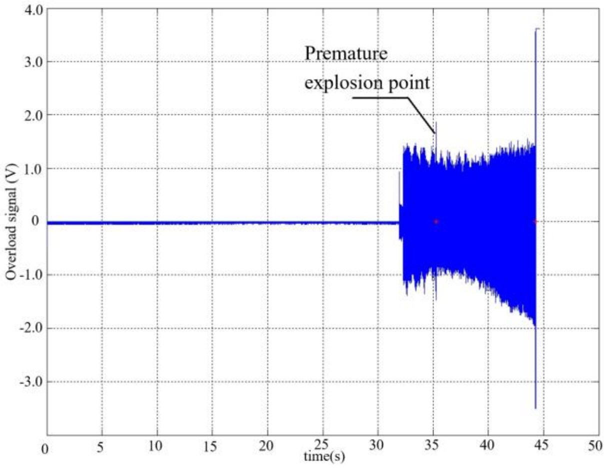

Figure 7. Data 1 full ballistic data chart.

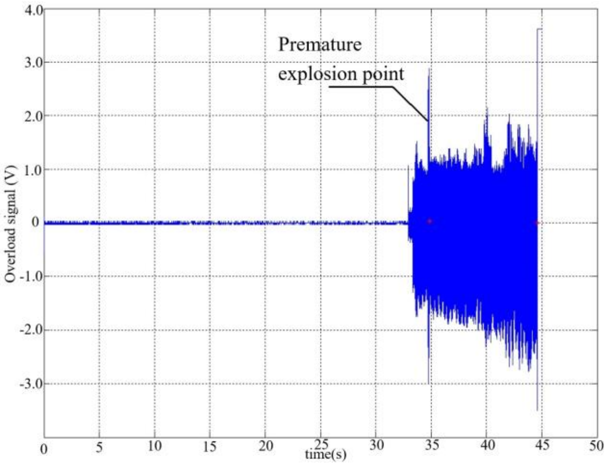

Figure 8. Full ballistic data chart.

3.3. Modal simulation results

Finite element modal analysis results indicate that the first-order bending mode natural frequency of the entire projectile body is approximately 501 Hz, as shown in Figure 9. The local bending mode natural frequency of the fuze section is approximately 1216 Hz, as shown in Figure 10. The vibration mode shape of this local mode indicates a tendency for strain concentration at the local structure. Its frequency band overlaps with the excitation band identified in Section 0, providing a clear target for subsequent modal test verification. Simulation results demonstrate high consistency between FTA and experimental modal analysis outcomes.

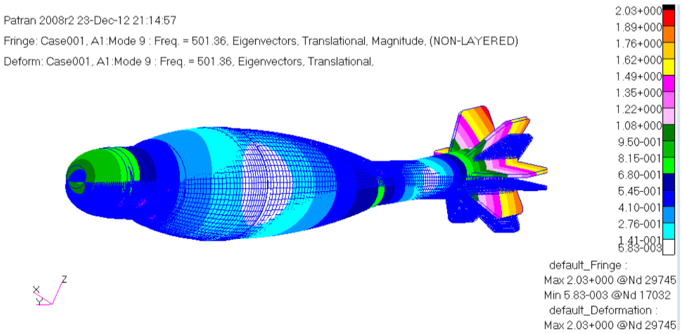

Figure 9. First bending mode frequency of the complete projectile.

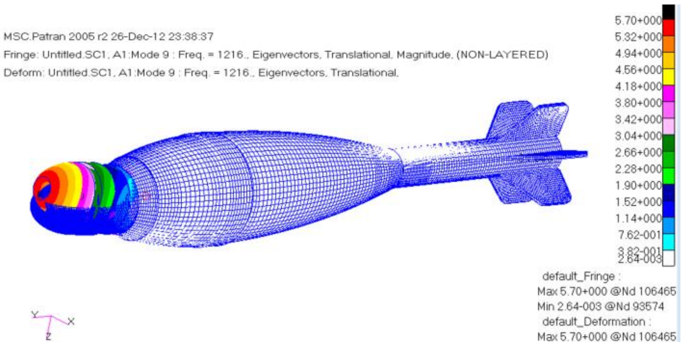

Figure 10. Local bending mode frequency of the fuze.

3.4. Experimental modal verification results

Impact hammer modal tests were conducted on five specimens (S1-S5) in their original state. The first three modal orders identified by the PolyMAX algorithm are summarized in Table 4, and Figure 11-20 shows the FRF, coherence function, and MAC plots.

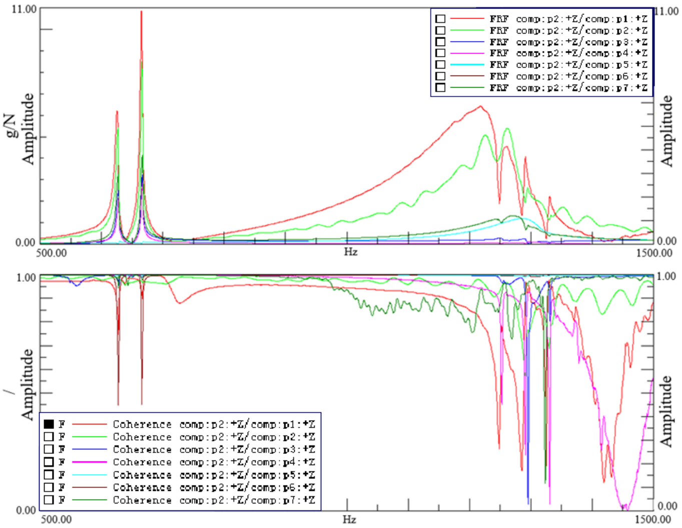

Figure 11. S1 frequency response function and coherence function.

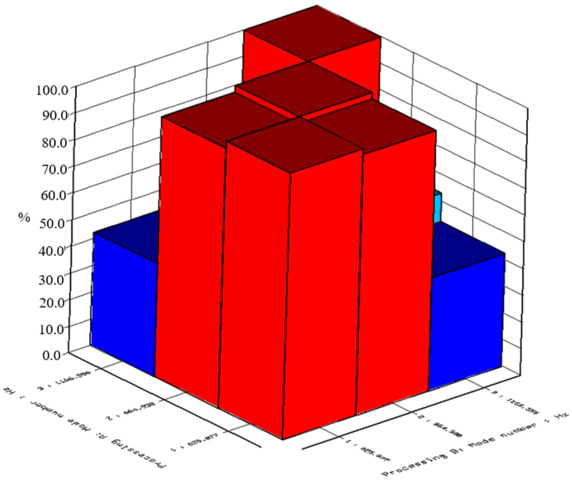

Figure 12. MAC diagram for S1.

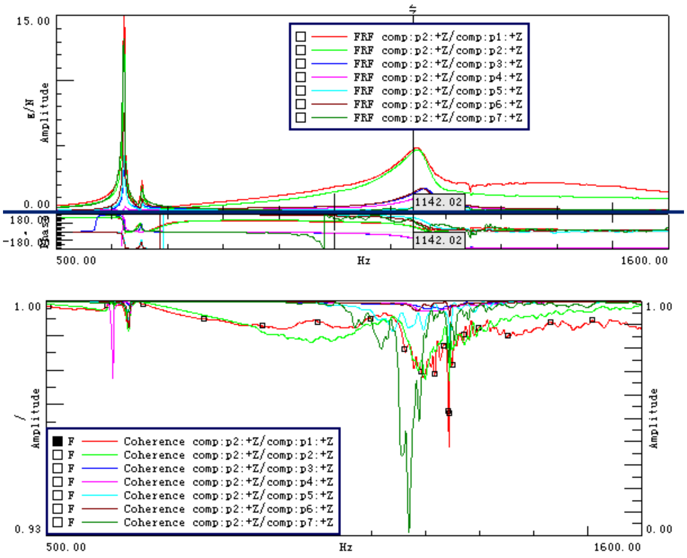

Figure 13. S2 frequency response function and coherence function.

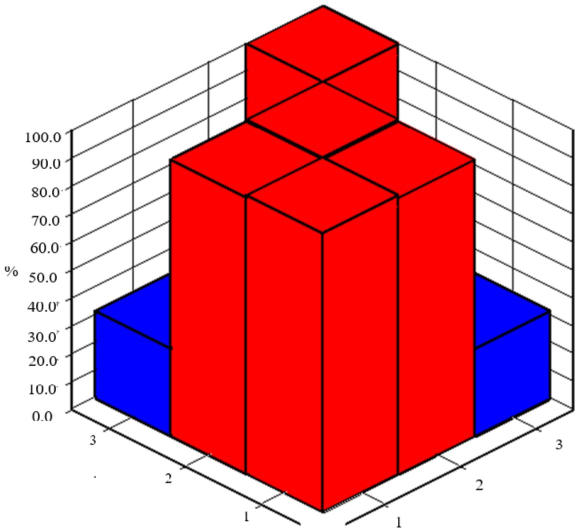

Figure 14. MAC diagram for S2.

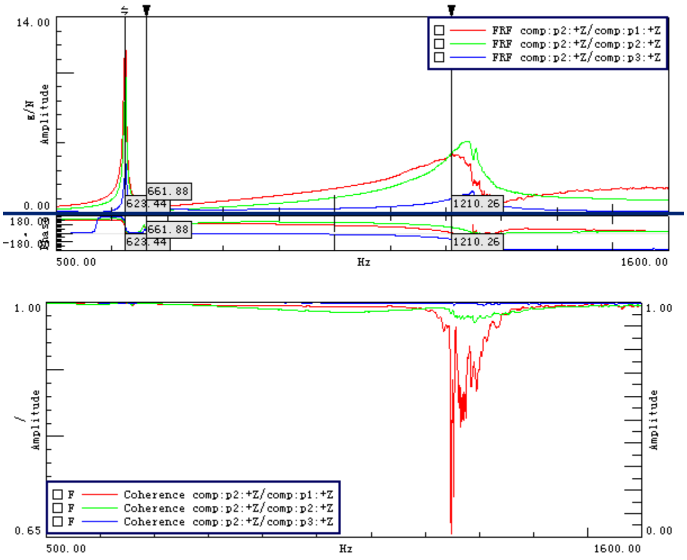

Figure 15. S3 frequency response function and coherence function.

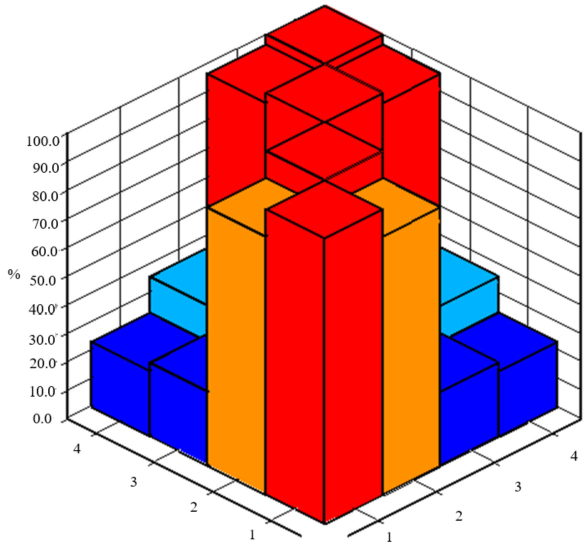

Figure 16. MAC diagram for S3.

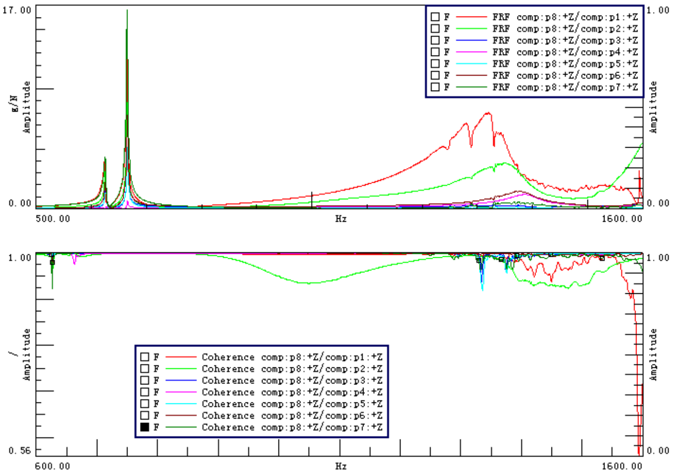

Figure 17. S4 frequency response function and coherence function.

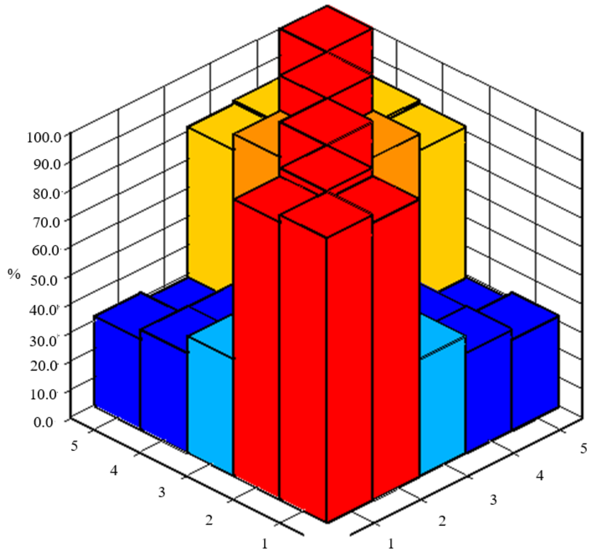

Figure 18. MAC diagram for S4.

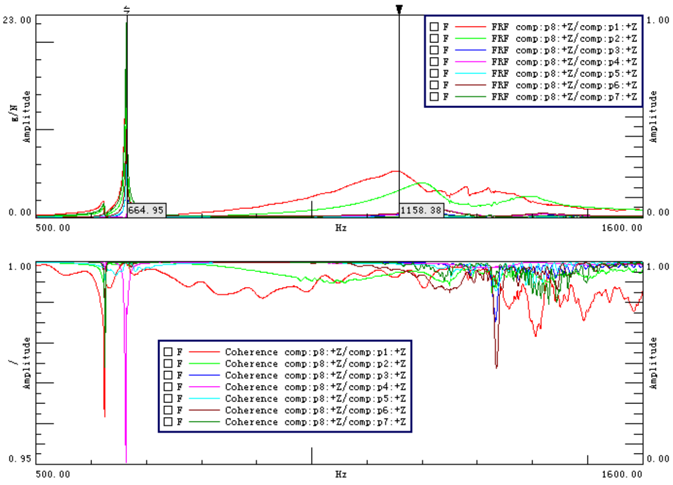

Figure 19. S5 frequency response function and coherence function.

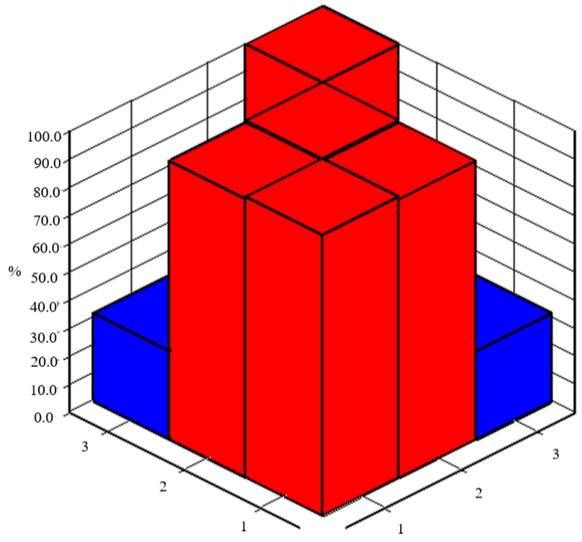

Figure 20. MAC diagram for S5.

The statistical results of the structural modal test for all states are shown in Table 4.

Table 4. Modal Test Results of the Original Structural State.

modal	Parameter/Uni	S1	S2	S3	S4	S5	Mean
Mode 1	Frequency (Hz)	625.9	616.8	623.8	624.7	624.6	623.2
	MOV(%)	100.0	100.0	100.0	100.0	100.0	100.0
	MAC(%)	100.0	97.4	98.0	88.6	97.4	96.3
	MPD(°)	0.0	9.5	7.5	19.4	26.5	12.6
Mode 2	Frequency (Hz)	664.9	650	661.9	663.6	663.2	660.7
	MOV(%)	100.0	100.0	99.5	100.0	100.0	99.9
	MAC(%)	100.0	98.6	99.7	96.6	98.6	98.7
	MPD(°)	0.0	7.2	3.5	10.0	16.9	7.5
Mode 3	Frequency (Hz)	1166.6	1165.6	1230.2	1266.8	1191.3	1204.1
	MOV(%)	100.0	100.0	98.7	100.0	100.0	99.7
	MAC(%)	100.0	90.6	99.2	97.2	90.6	95.5
	MPD(°)	0.0	20.2	9.1	9.2	12.5	10.2
	Amplitude (g/N)	5.05	5.00	5.11	5.11	4.47	4.95

Based on systematic modal test results of five specimens (Table 4), the data for each specimen at low-order modes are highly consistent. The first-order modal frequency ranges from 616.8–625.9 Hz, and the second-order ranges from 661.9–664.9 Hz, neither falling within the turbine generator excitation frequency band (1160–1240 Hz). The third-order mode, however, displays a frequency range of 1166.6–1266.8 Hz with a mean of 1204.10 Hz, representing an 8.2% relative dispersion. The mean value differs by only 4.1 Hz from the excitation band center (1200 Hz) and by 11.9 Hz (0.98%) from the finite element prediction (1216 Hz). MOV values exceeding 99% and MAC diagonal elements approaching unity confirm measurement reliability.

The elevated dispersion observed in the third-order mode arises from interface contact stiffness variations at the fuze-projectile threaded connection. In assembled structures with threaded joints, the equivalent stiffness governing local bending modes comprises structural stiffness and interface contact stiffness in series [39]. Interface contact stiffness depends on actual contact area and normal preload: dimensional variations of threaded interfaces due to manufacturing tolerances affect contact geometry, while assembly torque variations produce different preload magnitudes across specimens. Contact mechanics theory establishes that contact stiffness follows a power-law relationship with normal load [40], rendering modal frequencies sensitive to preload variations. The third-order mode involves local bending deformation concentrated at the interface, whereas the first two modes involve primarily global deformation patterns less affected by interface conditions. Despite this dispersion, all specimens exhibit third-order frequencies within or proximate to the excitation band, confirming that resonance risk exists across the production population rather than being confined to isolated units.

3.5. Resonance mechanism confirmation

Based on cross-verification of the four-layer evidence chain, structural resonance at the fuze-projectile interface is confirmed as the main fault source leading to ballistic premature detonation:

(1) Time-frequency evidence: Fault occurrence period is spatiotemporally synchronized with excitation frequency band.

(2) Simulaband.prediction: Local modal frequency predicted by FEA overlaps with excitation frequency band;

(3) Experimental verification: Measured frequency differs from simulation prediction by 0.98%, highly matching excitation frequency band.

Therefore, the conclusion is reached: structural resonance at the fuze-projectile interface is the primary fault source leading to ballistic premature detonation in this 82 mm mortar projectile fuze. Multi-source evidence cross-verification achieves high-confidence fault source confirmation under small-sample conditions. Compared to single methods, this study minimizes the risk of misdiagnosis through closed-loop verification of "phenomenon-theory-experiment". This multi-scale verification strategy has universal applicability for fault diagnosis of weapon equipment with high reliability requirements.

4. Vibration suppression strategy and engineering verification

4.1. Vibration suppression mechanism and strategy design

The fuze and projectile body are connected through threads, which can be equivalently modeled as a "spring-damper" parallel system. When a washer is added between the fuze and projectile body, the stiffness of axial force-transmitting components k_r, washer stiffness k_g, and contact stiffness k_c are connected in series [39]; meanwhile, internal friction of the washer material and interface micro-slip increase energy dissipation, enhancing equivalent damping. According to isolation and vibration reduction design principles—avoiding resonance zones by reducing stiffness and reducing peak response by increasing damping [8].

Its equivalent stiffness is:

$$k_{eq} = \left(\frac{1}{k_r} + \frac{1}{k_g} + \frac{1}{k_c}\right)^{-1} \tag{7}$$

Stiffness rearrangement causes the natural frequency shift to become:

$$f_0 = \frac{1}{2\pi}\sqrt{\frac{k_{\text{eq}}}{m}} \tag{8}$$

Friction dissipation at the washer interface can be described by the Coulomb damping model. Under harmonic excitation, the energy dissipated per cycle due to micro-slip at the interface is [41]:

$$\Delta E = W_d = 4\mu F_p \delta_{rel} \tag{9}$$

Here, μ represents the interfacial friction coefficient; δ_{rel} denotes the relative slip displacement at the interface.

For elastic connections, the relative slip is proportional to the vibration amplitude X; Based on the maximum elastic potential energy (energy storage) $E = \frac{1}{2}k_{eq}X^2$ [7] of the vibration system under steady-state harmonic motion and the relationship between dissipation and energy storage per cycle $\Delta E = 4\pi\zeta_{\text{eq}}E$, the equivalent damping ratio can be derived as:

$$\zeta_{\text{eq}} = \frac{2\mu\gamma F_p}{\pi k_{\text{eq}} X} \tag{10}$$

X represents the peak displacement of the structure (modal displacement amplitude), and γ denotes the dimensionless slip coefficient.

According to Equation (9), micro-slip at the interface and internal friction within the material convert mechanical energy into thermal energy during each vibration cycle. The dissipated power is proportional to the square of the vibration amplitude and the damping ratio. As per Equation (10), increasing the preload enhances the interface pressure, thereby strengthening the friction dissipation effect.

For the fuze-projectile resonance problem, vibration suppression approaches include: changing structural natural frequency (increasing or decreasing), adjusting excitation source characteristics, or enhancing interface dissipation. Considering that the fuze shape and mass are fixed, substantially changing natural frequency (requiring increase or decrease of about 1000 Hz) is not engineeringly feasible and has high cost; changing turbine generator speed is limited by bearing performance and electrical parameters.

Inserting elastic washers at the fuze-projectile contact surface reduces interface equivalent stiffness k_{eq}, causing local mode natural frequency f_0 to shift toward lower frequencies, thus moving sensitive modal frequency out of the excitation frequency band; under the same excitation, elastic performance introduced by the interface and friction dissipation generated by micro-slip will increase equivalent damping ratio ζ_{eq}, significantly reducing steady-state response peak. The passive vibration suppression approach adopted in this study offers practical ad-vantages over active control alternatives for expendable ordnance applications. Active vibration suppression systems require external power supplies, sensors, control electronics, and real-time feedback loops, introducing substantial complexity and cost [42]. Further-more, the harsh launch environment (high g-loads, propellant gas exposure) poses severe survivability challenges for active electronic components. The passive wave spring solution requires no electrical power, contains no fail-ure-prone electronics, and integrates seam-lessly into the existing assembly process. While active systems may achieve theoretically su-perior suppression performance under labora-tory conditions, the passive approach demon-strated here provides robust, predictable per-formance suitable for mass production and field deployment. The following sections will verify the effectiveness of this solution through multi-state comparative tests.

4.2. Vibration suppression effect evaluation

To validate the effectiveness of adding an elastic washer at the fuze-projectile interface, five vibration-damping modal tests with con-trolled assembly conditions were designed. These tests aimed to systematically quantify the impact of vibration-damping measures on structural dynamic characteristics, as shown in Table 4. State variables include preload force and presence/absence of washers, used to evaluate independent and coupled effects of connection stiffness and interface dissipation mechanisms. The baseline risk assessment uses the original ammunition configuration in State 1 (average values in Table 4 of Section 2.2.3.3). All tests strictly adhere to the data collection and processing procedures outlined in Section 2.2.3.1 to ensure data consistency and comparability.

Table 5. Test piece configuration status.

State No	Washer Configuration	Thread Preload
1	None	Natural installation
2	Only the upper part of the fuze is configured with a washer	Natural installation
3	Upper and lower side washers for the fuze	Natural installation
4	Upper and lower side washers for the fuze	Wrench-tightened
5	Only the upper part of the fuze is configured with a washer	Wrench-tightened

According to the conditions in Table 5, Hammering modal identification tests were conducted on states 2-5. The FRF and MAC diagrams are shown in Figures 21-28.

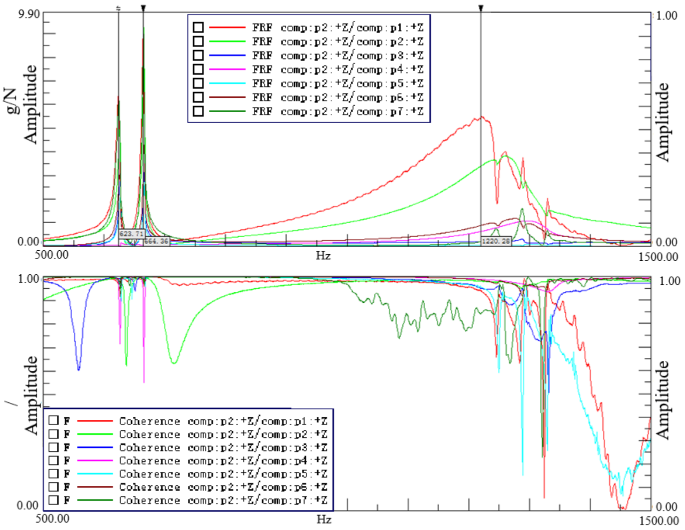

Figure 21. State-2 frequency response function and coherence function.

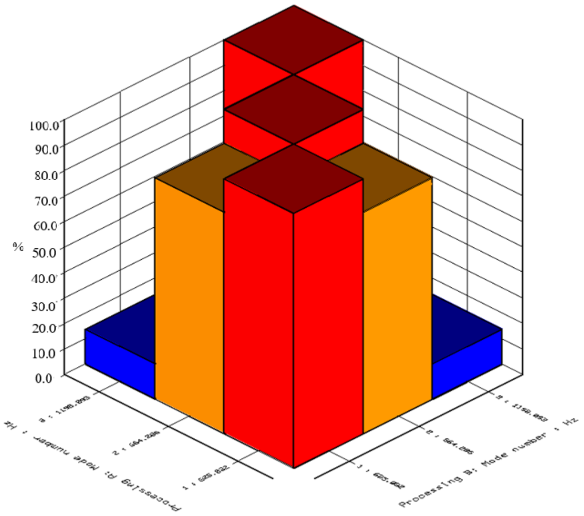

Figure 22. MAC diagram for State 2.

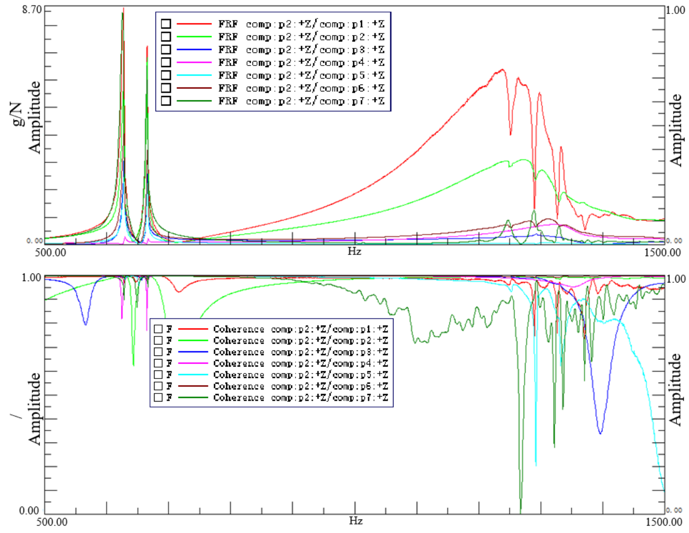

Figure 23. State-3 frequency response function and coherence function.

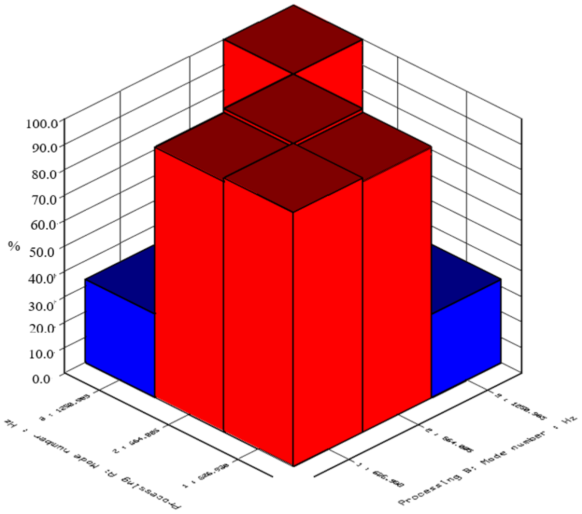

Figure 24. MAC diagram for State 3.

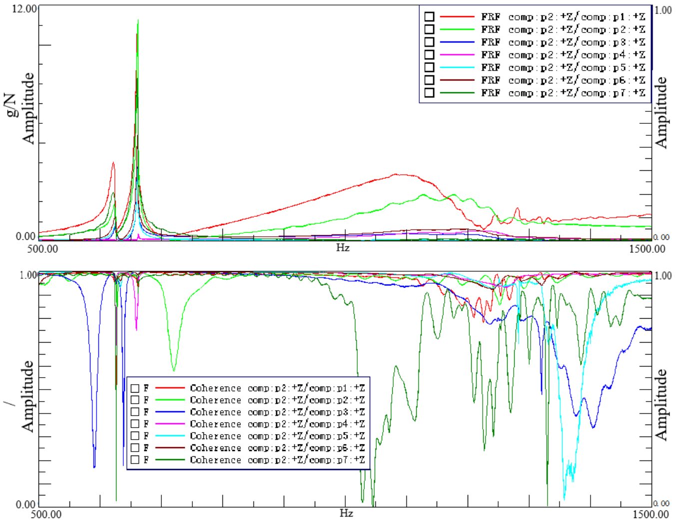

Figure 25. State-4 frequency response function and coherence function.

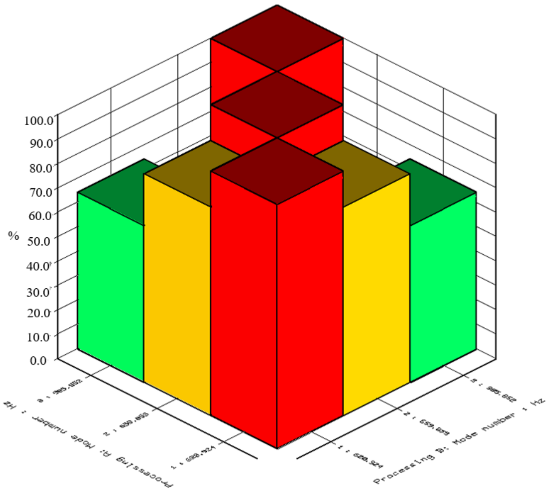

Figure 26. MAC diagram for State 4.

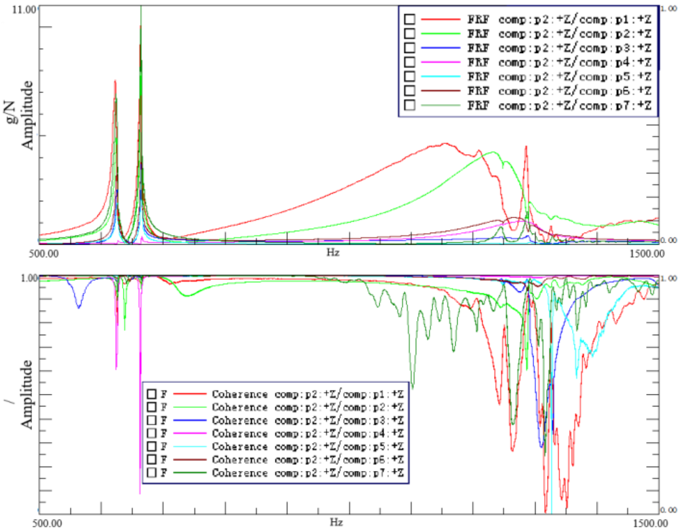

Figure 27. State-5 frequency response function and coherence function.

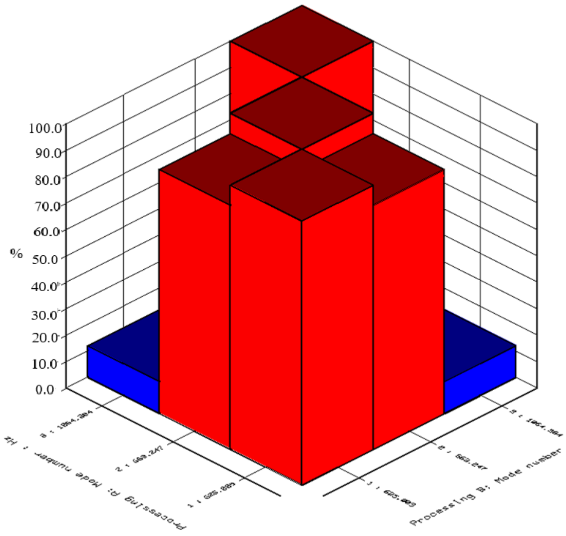

Figure 28. MAC diagram for State 5.

The statistical results of all states from the structural modal testing are shown in Table 6.

Table 6. Modal test results of specimens in different states.

Mode	Parameter/Unit	State 1	State 2	State 3	State 4	State 5
Mode 1	Frequency (Hz)	623.16	625	623.8	620.9	625.0
	MOV(%)	100.0	100.0	100.0	100.0	100.0
	MPC(%)	96.3	100.0	94.5	100.0	100.0
	MPD(°)	12.6	0.0	12.2	0.0	0.0
Mode 2	Frequency (Hz)	660.72	664.3	665.1	659.9	663.2
	MOV(%)	99.9	100.0	99.5	100.0	100.0
	MPC(%)	98.7	100.0	97.1	100.0	100.0
	MPD(°)	7.5	0.0.0v	10.7	0.0	0.0
Mode 3	Frequency (Hz)	1204.1	1198.1	1257.4	985.9	1064.4
	MOV(%)	99.7	100.0	98.7	100.0	100.0
	MPC(%)	95.5	100.0	94.6	100.0	100.0
	MPD(°)	10.20	0.0	16.3	0.0	0.0
	Amplitude (g/N)	4.95	3.80	3.00	2.20	4.10

To systematically evaluate the impact of assembly conditions on modal characteristics, Table 7 summarizes the third-order modal parameters across five states. Particular attention is given to the third-order mode, which corresponds to the local bending mode pre-dicted by finite element simulation and repre-sents a potential resonance risk source.

Table 7. Comprehensive comparison results of multi state modal testing.

State	Vibration Suppression Measure	3rd Order Freq (Hz)	Relative Baseline Freq Shift (Hz)	Relative Baseline Freq Shift Rate	Amplitude (g/N)	Amplitude Change Rate
1 (Baseline)	None	1204.1	--	--	4.95	--
2	Single-side washer	1198.1	-6	-0.50%	3.80	-23.23%
3	Bilateral washers	1257.4	53.3	4.43%	3.00	-39.39%
4	Bilateral washers + tightening	985.9	-218.2	-18.12%	2.20	-55.56%
5	Single washer + tightening	1064.4	-139.7	-11.60%	4.10	-17.17%

FromTable 6, all states have MOV values greater than 95% and MAC values greater than 94%, ensuring test result reliability. According to Table 7, the first two modes are far from the resonance frequency band, so the influence of the first two modes is ignored here. For the third-order mode, the natural frequency variation range is 985.9-1257.4 Hz, with frequency fluctuation reaching 271.5 Hz (21.6%). State 1→State 2: after adding only a single-side washer, frequency change is small, amplitude decreased by 23.23%; State 1→State 3: after adding bilateral washers, frequency increased, amplitude decreased by 39.39%, indicating that bilateral washer configuration significantly improves dissipation efficiency compared to single-side; State 1→State 5: frequency shifted down 11.60%, amplitude decreased 17.17%, indicating single-side washer + "wrench tightening" vibration suppression effect is better than single-side alone but inferior to bilateral configuration; State 1 →State 4: frequency shifted down 18.12%, amplitude decreased 55.56%, with maximum reductions in both frequency and amplitude. Therefore, pure stiffness regulation or pure interface dissipation has limited effect; synergistic action of both achieves optimal vibration suppression; State 4 uses dual measures, balancing "no resonance" (frequency shift) and "small response" (damping peak reduction), proving superiority of "stiffness regulation + energy dissipation" synergistic strategy.

4.3. Vibration suppression optimization

4.3.1. Wave spring design

The wave spring configuration was se-lected based on its tunable stiffness character-istics. Unlike flat washers that provide negli-gible axial deflection, wave springs exhibit adjustable stiffness governed by geometric parameters including wave number, ampli-tude, and material thickness [43]. This tuna-bility enables targeted modification of inter-face stiffness to shift the assembly natural frequency away from the excitation band—a capability that flat washers fundamentally cannot provide.

Based on the verification test results pre-sented in Section 4.2, the addition of elastic washers demonstrated a significant resonance suppression effect. To further reduce the reso-nance amplitude and achieve a uniform distri-bution of force in the circumferential direc-tion, two redesigned single-layer wave springs featuring openings and three waves were em-ployed. The configuration of these springs is illustrated in Figure 29: (a) depicts the washer between the fuze lower body and the joint screw, (b) shows the washer at the joint-screw interface, with (c) and (d) being their respec-tive developed views. The wave springs were fabricated from 65Mn spring steel conforming to Chinese national standard GB/T 1222-2016 [44]. Mechanical properties of this mate-rial, as specified in GB/T 699-2015 [45], in-clude an elastic modulus of 211 GPa, shear modulus of 83.67 GPa, yield strength no less than 430 MPa, ultimate tensile strength no less than 735 MPa, and density of 7.81 g/cm^3.

The principal vibration suppression mechanism in the proposed design does not rely on material damping. Rather, suppression is achieved through a combination of interface stiffness modification, which shifts the modal frequency away from the excitation band, and frictional energy dissipation at the spring-component contact interfaces. Experimental modal testing results presented in Section 3 confirm the effectiveness of this mechanism.

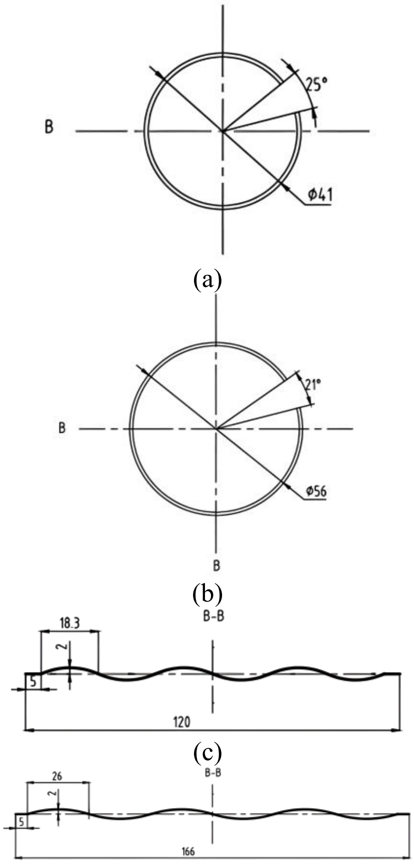

(a)

(b)

(c)

(d)

Figure 29. Design Drawings of Two Types of Wave Springs.

4.3.2. Wave spring effect modal test verification

In order to verify the dissipation effect of the waveform spring interface, modal tests were conducted on five samples (N1-N5) with waveform springs according to the testing method in Section 2.2.3, and the results summarized in Table 8 and Table 9 were obtained (Figure 30-34).

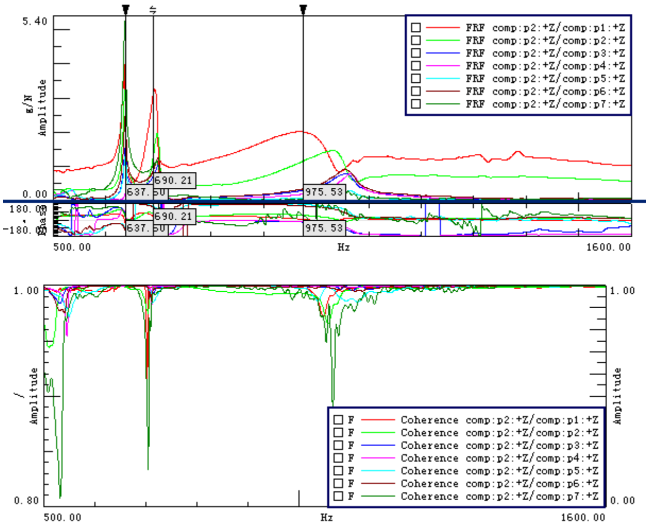

Figure 30. N1 frequency response function and coherence function.

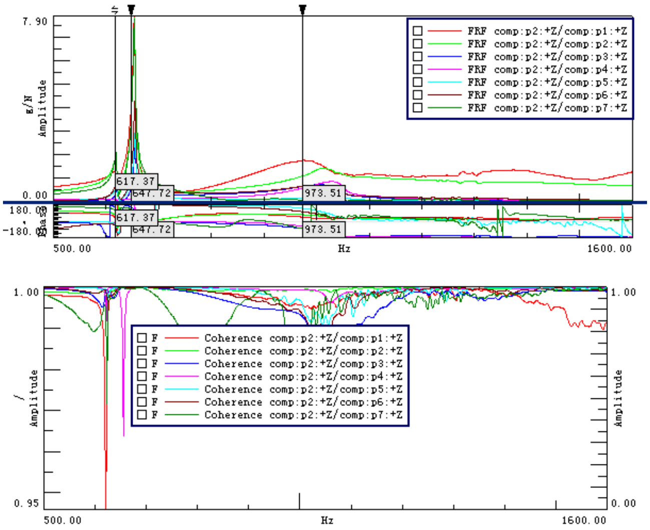

Figure 31. N2 frequency response function and coherence function.

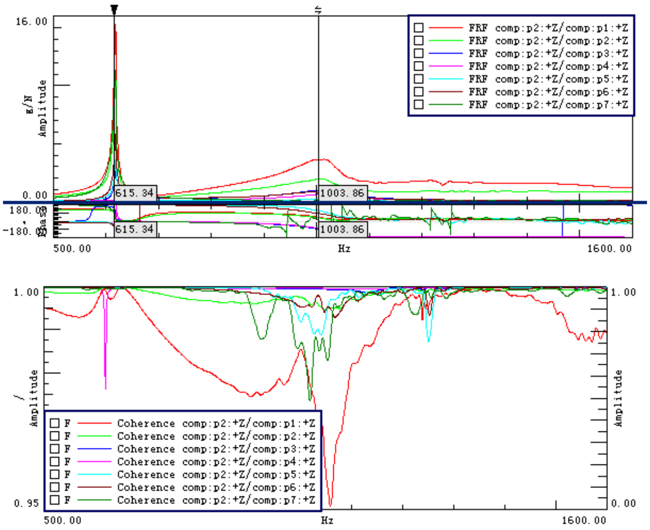

Figure 32. N3 frequency response function and coherence function.

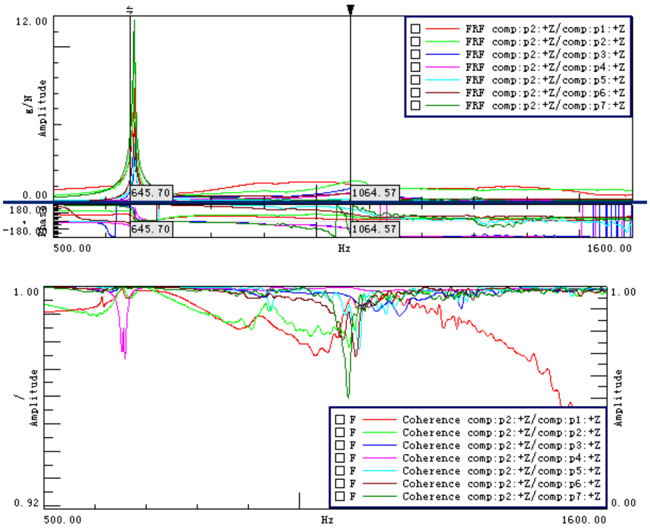

Figure 33. N4 frequency response function and coherence function.

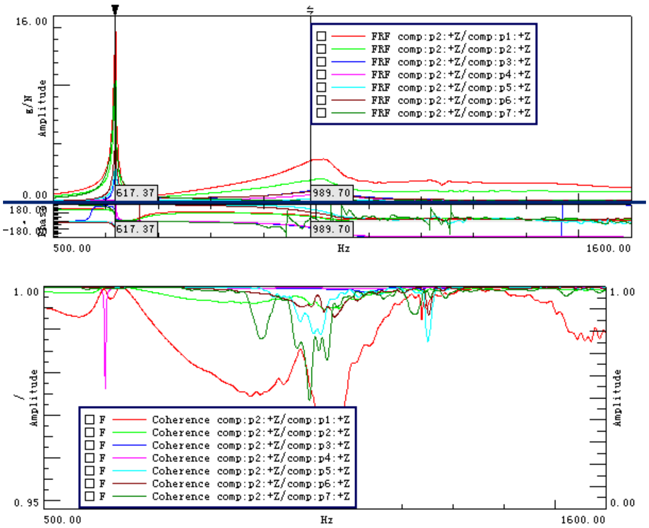

Figure 34. N5 frequency response function and coherence function.

The statistical results of all numbered modal tests with added waveform springs are shown in Table 8.

Based on the superiority of the “stiffness control + interface dissipation” strategy, the vibration suppression measure was modified to incorporate double-sided wave springs. The test results (Table 8) indicate that the frequency range remained relatively stable between 987.2 and 1064.6 Hz, accompanied by a significant amplitude reduction with a maximum decrease of 1.78 g/N. As revealed in Table 9, the third-order modal frequency decreased by 17.73% relative to the center of the turbine generator's excitation band and by up to 19.98% compared to the original structure's average frequency. When compared to State 4 (featuring dual washers), the maximum frequency increase was 7.98%. Although frequencies increased, they shifted away from the excitation band. The maximum amplitude reduction reached 73.06% relative to the baseline (State 1), and 39.39% relative to State 4. The wave spring achieves dual enhancements in assembly stability and dissipation efficiency through its nonlinear stiffness characteristics and the promotion of interface micro-slip.

Following wave spring installation, the third-order modal frequencies of all specimens shifted to the range of 987.2–1064.6 Hz (Table 8), with a reduced relative dispersion of approximately 7.6% compared to the original state (8.2%). This reduction can be explained by the dominant role of wave spring stiffness in interface dynamic behavior, which reduces the sensitivity of modal frequencies to variations in other assembly parameters. Importantly, all post-modification frequencies lie below the lower bound of the excitation band (1160 Hz), demonstrating the robustness of the proposed vibration suppression scheme against production variability.

A comparison between flat washer configurations (States 2–5, Section 4.2) and the optimized wave spring configuration reveals the advantages of the wave spring design. With bilateral flat washers under wrench-tightened conditions (State 4), the third-order modal frequency reached 985.9 Hz with amplitude reduction of 55.56%. However, the frequency variation across different assembly states with flat washers was substantial, ranging from 985.9 Hz to 1257.4 Hz (271.5 Hz span), indicating high sensitivity to assembly conditions.In contrast, the wave spring configuration achieved third-order frequencies in the range of 987.2–1064.6 Hz across five specimens, with a reduced span of 77.4 Hz and additional amplitude reduction of 39.39% relative to State 4. The wave springs thus provide more consistent frequency control with lower sensitivity to production and assembly variations, while delivering enhanced vibration attenuation through the combined mechanisms of stiffness modification and interface friction dissipation.

Table 8. Modal Test Results with Wave-Spring Retrofit.

No.	Washer State	Joint-Screw Installation State	3rd Order Freq(Hz)	Amplitude(g/N)
N1	Bilateral wave spring washers	Wrench-tightened	987.2	1.46
N2	Bilateral wave spring washers	Wrench-tightened	1005.5	1.50
N3	Bilateral wave spring washers	Wrench-tightened	1010.4	1.78
N4	Bilateral wave spring washers	Wrench-tightened	1064.6	1.33
N5	Bilateral wave spring washers	Wrench-tightened	999.5	1.78

Table 9. Modal Synthesis Comparison Results with Wave-Spring Retrofit.

No.	Relative to Excitation Band Center	Relative Baseline Freq Shift Rate	Relative State 4 Freq Shift Rate	Relative Baseline Amplitude Change Rate	Relative state 4 amplitude change rate
N1	-17.73%	-21.18%	0.13%	-70.56%	-33.77%
N2	-16.21%	-19.39%	1.99%	-69.60%	-31.60%
N3	-15.80%	-18.91%	2.49%	-64.09%	-19.19%
N4	-11.28%	-13.62%	7.98%	-73.06%	-39.39%
N5	-16.71%	-19.98%	1.38%	-64.09%	-19.19%

4.3.3. Results of the wave spring firing tests

Range tests were conducted at a certain test range using XX87-type 82 mm mortar projectiles at normal temperature, with test results shown in Table 10. For charge 0 at a 45-degree firing angle, 10 rounds were tested and all functioned properly; for charge 4 at a 78-degree firing angle, 10 rounds were tested (5 at high burst height and 5 at low burst height), and all functioned properly; for charge 6 at a 76-degree firing angle, 10 rounds were tested (5 at high burst height and 5 at low burst height), and all functioned properly. The software and hardware states of the electronic components were consistent with those in the engineering prototype quali-fication tests, with only structural modifica-tions of adding two wave springs bilaterally and tightening the threaded connections with a wrench, while all other aspects remained un-changed.

Table 10. Range Test Results.

Serial No.	Projectile Type	Ambient Temp	Charge No.	Firing Angle (°)	Rounds Fired	Action Result
1	82mm mortar projectile	Normal temp	0	45	10	functioned properly
2	Same as above	Normal temp	4	78	10	functioned properly
3	Same as above	Normal temp	6	76	10	functioned properly
4	Same as above	Normal temp	6	58	10	functioned properly

Range test results show that the wave spring solution is effective under different charge numbers (0/4/6) and firing angles (45°-78°). The strategy of adding wave springs bilaterally to the fuze-projectile body is effective and solves the fuze ballistic premature detonation problem induced by structural resonance.

5. Conclusions

Targeting the ballistic early-detonation problem in a certain type of 82mm mortar projectile fuze, this research has constructed a multi-scale analysis framework of "fault tracing- time-frequency mining - numerical simulation - experimental modal validation " The following conclusions are drawn:

(1) Resonance between the fuze-projectile interface local bending mode and the turbine generator excitation frequency band is identified as the primary cause of ballistic premature detonation. The four-layer evidence chain consisting of fault tree analysis, full-trajectory time-frequency mining, finite element prediction, and modal testing confirms the resonance triggering mechanism, achieving high-confidence fault source identification.

(2) Assembly parameters exert significant regulatory effects on fuze high-frequency modes. Thread preload and washer configuration significantly affect interface stiffness and damping characteristics. Multi-state comparative tests quantify the regulatory patterns of these two factors on modal frequency, providing quantitative basis for controlling structural dynamic characteristics through assembly processes.

(3) The "stiffness regulation—interface dissipation" synergistic vibration suppression strategy effectively eliminates ballistic premature detonation risk. The bilateral washer configuration shifts the modal frequency out of the excitation band, while interface dissipation significantly reduces response amplitude. The wave spring optimization scheme further enhances frequency stability and damping effectiveness. Live-fire range tests validate the robustness of this strategy under various operating conditions.

(4) The multi-scale validation framework can accurately diagnose faults under small sample conditions. The vibration suppression scheme is low-cost, easy to implement, and highly reliable, providing engineering basis for the assembly optimization and reliability improvement of weapon systems.

The engineering effectiveness of the proposed methodology is demonstrated by the following quantified outcomes:

(1) the premature detonation failure rate was reduced from 5.5% (5 of 91 rounds) to 0% (0 of 40 rounds) in field verification tests;

(2) the third-order modal frequency was shifted by 18.1% below the excitation band center, from 1204.1 Hz to 985.9 Hz with bilateral washers and wrench-tightening;

(3) vibration response amplitude was reduced by 55.6% (from 4.95 g/N to 2.2 g/N) with bilateral washers, and further reduced to an average of approximately 1.57 g/N

with optimized wave springs;

(4) the solution requires only two additional low-cost components (wave springs) with no modification to fuze electronics or projectile structure.

This study has certain limitations that warrant acknowledgment. Live-fire verification was conducted only under normal temperature conditions (15–25°C); environmental qualification testing across the military temperature range (−40°C to +60°C) is recommended in future work to validate robustness under extreme service conditions. Additionally, while the analytical framework is generalizable to other ammunition systems, the methodology was demonstrated specifically for 82 mm mortar projectile fuzes; validation for other calibers and fuze configurations would strengthen universality claims.

References

1. Mitura A, Gawryluk J. Experimental and finite element analysis of PPF controller effectiveness in composite beam vibration suppression. Eksploatacja i Niezawodnosc – Maintenance and Reliability 2022; 24(3): 468–477. https://doi.org/10.17531/ein.2022.3.8.
2. Wang H, Wang Y, Xu J, Qin H. Fatigue strength reliability assessment of turbofan blades subjected to intake disturbances based on the improved kriging model. Eksploatacja i Niezawodnosc – Maintenance and Reliability 2025; 27(2): 194175. https://doi.org/10.17531/ein/194175.
3. Wang J W, Wang Y S, Wang G Y. A review of fuze ballistic burst accidents and their causes in world. Journal of Detection & Control 2025; 1-13. Available from: https://link.cnki.net/urlid/61.1316.TJ.20241225.1507.002.
4. Xue M, Wen R, Chen W, Wei Z. Overview of the design methods of electromagnetic compatibility in electronic systems of fuzes. In: 2024 14th International Symposium on Antennas, Propagation and EM Theory (ISAPE); 2024 Oct 23-26; Hefei, China. IEEE 2024; 1–3. https://doi.org/10.1109/ISAPE62431.2024.10840931.
5. Xu H M, Wang Y S, Wen Q. Optimal selection of material for interrupter structure part of fuze. Journal of Detection & Control 2025; 1–13. https://link.cnki.net/urlid/61.1316.TJ.20250424.1258.002.
6. Zhang H. Application prospect of vibration and shock in fuze technology. Journal of Vibration, Measurement & Diagnosis 2019; 39: 235–241+438. https://doi.org/10.16450/j.cnki.issn.1004-6801.2019.02.001.
7. Den Hartog J P. Mechanical vibrations. New York: McGraw-Hill; 1956.
8. Harris C M, Piersol A G, editors. Harris' shock and vibration handbook. 5th ed. New York: McGraw-Hill; 2002.
9. Ewins D J. Modal testing: theory, practice and application. 2nd ed. Baldock, UK: Research Studies Press, LTD; 2001.
10. Zhang W F, Wang YS, Zhang H, Li C L. Analysis of inertial impact switch dynamic characteristics and fuze ballistic explosion. Journal of Detection & Control 2016; 38(3): 35–40. https://doi.org/CNKI:SUN:XDYX.0.2016-03-008.
11. Al-Haddad L A, Giernacki W, Shandookh A A, Jaber A A, Puchalski R. Vibration signal processing for multirotor UAVs fault diagnosis: filtering or multiresolution analysis? Eksploatacja i Niezawodnosc – Maintenance and Reliability 2024; 26(1): 176318. https://doi.org/10.17531/ein/176318.
12. Chen K, Yang C, Zhao Y, Niu P, Niu N, Wu H. Optimization of square-shaped bolted joints based on improved particle swarm optimization algorithm. Eksploatacja i Niezawodnosc – Maintenance and Reliability 2023; 25(3): 168487. https://doi.org/10.17531/ein/168487.
13. Chen G, Chen Y, Chen Y, Ji S. Dynamics modeling and experimental modal analysis of bolt loosening for lightning rod. Journal of Vibroengineering 2020; 22(3): 657–671. https://doi.org/10.21595/jve.2019.20918.
14. Guo H, Zhong J, Feng B, Chen Y, Zhong S. Detection method for bolt loosening based on summation coefficient of absolute spectrum ratio. Sensors 2025; 25(1): 246. https://doi.org/10.3390/s25010246.
15. Zhang H, Chen T, Ji K, Zhu M, Ju C. Study on preload of bolted connections in pitch bearing based on vibration modal analysis. Shock and Vibration 2023; 2023: 6653564. https://doi.org/10.1155/2023/6653564.
16. Yuan J, Gastaldi C, Denimal E, Chouvion B. Friction damping for turbomachinery: a comprehensive review of modelling, design strategies, and testing capabilities. Progress in Aerospace Sciences 2024; 144: 101018. https://doi.org/10.1016/j.paerosci.2024.101018.
17. Yan Y M, Zhou J Y, Yin Y, Nie H, Wei X H, Liang T T. Reliability estimation of retraction mechanism kinematic accuracy under small sample. Eksploatacja i Niezawodnosc – Maintenance and Reliability 2024; 26(1): 174777. https://doi.org/10.17531/ein/174777.
18. Zhang R, Song S. Bayesian network approach for dynamic fault tree with common cause failures and interval uncertainty parameters.

Eksploatacja i Niezawodnosc – Maintenance and Reliability 2024; 26(4): 190379. https://doi.org/10.17531/ein/190379.

19. Hsu T Y, Shih Y C, Pham Q V. Damage detection of a thin plate using modal curvature via macrostrain measurement. Earthquake Engineering and Engineering Vibration 2019; 18(2): 409–424. https://doi.org/10.1007/s11803-019-0512-y.
20. Magalhaes F, Cunha A, Caetano E. Vibration based structural health monitoring of an arch bridge: from automated OMA to damage detection. Mechanical Systems and Signal Processing 2012; 28: 212–228. https://doi.org/10.1016/j.ymssp.2011.06.011.
21. Navabian N, Bozorgnasab M, Taghipour R. Damage identification in plate-like structure using mode shape derivatives. Archive of Applied Mechanics 2016; 86: 819–830. https://doi.org/10.1007/s00419-015-1064-x.
22. Wei L, Peng X, Cao Y. Multi-scale graph transformer for rolling bearing fault diagnosis. Eksploatacja i Niezawodnosc – Maintenance and Reliability 2025; 27(2): 194779. https://doi.org/10.17531/ein/194779.
23. Peeters B, Van der Auweraer H, Guillaume P, Leuridan J. The PolyMAX frequency-domain method: a new standard for modal parameter estimation. Shock and Vibration 2004; 11: 395–409. https://doi.org/10.1155/2004/523692.
24. National Research Council. Reliability Growth: Enhancing Defense System Reliability. Washington DC: The National Academies Press; 2015.
25. General Armament Department of the PLA. Test methods of environmental and performance for fuze and fuze components: GJB 573B—2020. Beijing: Military Standards Publishing and Distribution Department of the General Armament Department; 2020. Chinese.
26. Sharp A, Andrade J, Ruffini N. Design for reliability for the high reliability fuze. Reliability Engineering and System Safety 2019; 181: 54–61. https://doi.org/10.1016/j.ress.2018.04.032.
27. Ma G S, He G L, Guo Y C. Research on natural frequency based on modal test for high speed vehicles. AIP Conference Proceedings 2018; 1955: 030059. https://doi.org/10.1063/1.5033658.
28. Li X, Zhang D M, Zhao K N. Common problems analysis of impact modal test in aeroengine component. Aeroengine 2010; 36(3): 47–51.
29. International Electrotechnical Commission. IEC 61025: Fault tree analysis (FTA). Geneva, Switzerland: International Electrotechnical Commission; 2006.
30. General Armament Department. Handbook for fuze typical fault tree: GJB/Z 29A-2003. Beijing: Commission of Science, Technology and Industry for National Defense 2003; 6–150. Chinese.
31. General Armament Department. Bottom-event data handbook for fuze fault tree: GJB/Z 179-2015. Beijing: Commission of Science, Technology and Industry for National Defense 2015; 1–27. Chinese.
32. Huo L N, Wang Y S. Fuze ballistic burst estimation by fault tree analysis. Journal of Detection & Control 2020; 42(6): 13–20.
33. Zhang J, Zhang W. Abnormal function reason analysis of a certain type of fuze delay mechanism. Equipment Manufacturing Technology 2021; (7): 236–239. https://doi.org/CNKI:SUN:GXJX.0.2021-07-061.
34. Peeters B, Van der Auweraer H. PolyMAX: a revolution in operational modal analysis. In: Proceedings of the 1st International Operational Modal Analysis Conference (IOMAC 2005); 2005 Apr 26-27; Copenhagen, Denmark. Aalborg: Aalborg Universitet; 2005.
35. Jiao B Q, Cao J X, Lu BJ, Li M, Liu PF. Modal test of shaft-mounted brake disc based on PolyMax modal parameter identification method. China Railway Science 2020; 41(4): 102–107.
36. Van der Auweraer H, Leurs W, Mas P, Hermans L. Modal parameter estimation from inconsistent data sets. In: Proceedings of the 18th International Modal Analysis Conference (IMAC XVIII); 2000 Feb 7-10; San Antonio, TX, USA. Bethel, CT: Society for Experimental Mechanics; 2000; 763–771.
37. Heylen W, Lammens S, Sas P. Modal analysis theory and testing. Translated by Bai H, Guo J; proofread by Tu L. Beijing: Beijing Institute of Technology Press; 2001.
38. Kinsler L E, et al. Fundamentals of acoustics. 4th ed. New York: Wiley; 2000.
39. Hu H Y. Fundamentals of mechanical vibration. Harbin: Harbin Institute of Technology Press; 2004; 13. Chinese.
40. Pohrt R, Popov V L. Contact stiffness of randomly rough surfaces. Scientific Reports 2013; 3: 3293. https://doi.org/10.1038/srep03293.
41. Stutts DS. Equivalent viscous damping. Rolla (MO): Missouri University of Science & Technology 2009. Available from: https://web.mst.edu/~stutts/supplementalnotes/eqivalentviscousdamping.pdf.
42. Diez-Jimenez E, Rizzo R, Gómez-García M J, Corral-Abad E. Review of Passive Electromagnetic Devices for Vibration Damping and Isolation. Shock and Vibration 2019; 2019: 1250707. https://doi.org/10.1155/2019/1250707.

43. Pedersen N L, Klit P. Wave spring stiffness and improved design. Journal of Strain Analysis for Engineering Design 2025; 60(8): 586–595. doi:10.1177/03093247251349565.
44. Standardization Administration of China. Spring steels: GB/T 1222-2016. Beijing: Standards Press of China; 2016. Chinese.
45. Standardization Administration of China. Quality carbon structural steels: GB/T 699-2015. Beijing: Standards Press of China; 2015. Chinese.

Nomenclature

Abbreviation	Description
FTA	Fault Tree Analysis
FEA	Finite Element Analysis
MAC	Modal Assurance Criterion
MOV	Modal Overcomplexity
MPC	Modal Phase Collinearity
FRF	frequency response function